nature communications

Article

https://doi.org/10.1038/s41467-025-61376-y

High-entropy alloyed single-atom Pt for methanol oxidation electrocatalysis

Received: 28 October 2024

Accepted: 20 June 2025

Published online: 10 July 2025

Check for updates

Mingda Liu[1,2,6], Zhichao Zhang[3,6], Chenyu Li[1,2], Sen Jin[1,2], Kunlei Zhu[4], Shoushan Fan[5], Jia Li[3] ✉ & Kai Liu[1,2] ✉

The methanol oxidation reaction is the bottleneck for direct methanol fuel cells. Unfortunately, the state-of-the-art Pt-based catalysts suffer heavily from the CO poisoning problem. Isolating Pt atoms in a material can avoid CO poisoning. However, single-atom Pt catalysts alone are inert towards methanol oxidation reaction. Here, we report high-entropy alloyed single-atom Pt catalysts, in which single-atom Pt sites are alloyed with non-noble elements in a high-entropy structure. This catalyst not only possesses active Pt sites but also inherits the ability of single-atom Pt to resist CO poisoning. Consequently, the catalyst shows a notable mass activity of 35.3 A mg^{-1} at only 2.3 at% Pt and maintains high activity even after operation for 180,000 s. Both experimental and theoretical results reveal that the high-entropy structure induces a synergistic effect, wherein the elements coordinated around single-atom Pt sites effectively remove adsorbed CO from Pt. This mechanism facilitates the key reaction steps of methanol oxidation reaction and avoids CO poisoning. This work presents a high-entropy alloyed single-atom strategy to realize efficient and durable methanol oxidation reaction catalysis with low costs.

The extensive extraction and use of fossil fuels have caused serious negative impacts on the environment. Consequently, the development of renewable and environment-friendly alternative energy sources is essential[1–3]. Since the early 1950s, direct methanol fuel cells (DMFCs) have attracted widespread attention because of their environmental friendliness, high energy density, low cost, and portability[4–7]. There are two crucial semi-reactions in DMFCs: the methanol oxidation reaction (MOR) at the anode and the oxygen reduction reaction (ORR) at the cathode. To date, ORR, which plays an important role in fuel cells and metal-air batteries, is relatively mature. By contrast, MOR, which involves complex six-electron transfer processes and exhibits more sluggish kinetics, is considered to be the bottleneck of DMFCs[5]. It is widely accepted that the MOR has a dual-pathway mechanism entailing an indirect CO pathway and direct CO-free pathway[4,5,7]. Although Pt remains the state-of-the-art active catalyst for MOR, it is expensive and suffers heavily from the poisoning problem in MOR due to the inevitable occurrence of CO pathway on Pt surface and the strong binding between CO intermediates and Pt, blocking active sites and impeding the reaction process[8–11]. Ideal MOR catalysts require simultaneous high mass activity (MA) and anti-CO poisoning capability[1,7,12,13].

Numerous studies have shown that the formation of *CO in MOR requires at least three contiguous Pt atoms[11,14,15]. Consequently, decreasing the Pt content, or ideally isolating Pt atoms in a material should suppress the CO pathway and avoid CO poisoning. In this regard, single-atom Pt (SA-Pt) is a potential poisoning-free MOR catalyst. However, SA-Pt alone has little or no MOR activity because it cannot activate C–O bonds[16–19]. The MOR catalytic activity of SA-Pt has been increased by adjusting its coordination environment, e.g., dispersing SA-Pt on precious-metal substrates like Ru or RuO_2[20,21].

[1]Key Laboratory of Advanced Materials (MOE), School of Materials Science and Engineering, Tsinghua University, Beijing 100084, P. R. China. [2]State Key Laboratory of New Ceramic Materials, Tsinghua University, Beijing 100084, P. R. China. [3]Shenzhen Geim Graphene Center and Institute of Materials Research, Tsinghua Shenzhen International Graduate School, Tsinghua University, Shenzhen 518055, P. R. China. [4]Department of Physics, Qufu Normal University, Qufu, Shandong 273165, P. R. China. [5]Department of Physics, Tsinghua University, Beijing 100084, P. R. China. [6]These authors contributed equally: Mingda Liu, Zhichao Zhang. ✉e-mail: li.jia@sz.tsinghua.edu.cn; liuk@tsinghua.edu.cn

However, these methods are expensive and have limited capability to improve the activity of SA-Pt.

High-entropy alloys (HEAs), which generally consist of five or more distributed elements in a single phase[15,22–24], are emerging as MOR catalysts. The cocktail effect induced by the alloying of multiple elements provides multiple active sites and regulates the adsorption energy of reaction intermediates[25–27]. Some Pt-containing HEA catalysts display relatively high MOR activity[22]. However, current HEA catalysts still require Pt to facilitate the mixing of elements or form intermetallic compounds. This situation results in contiguous Pt atoms in the HEA lattice, and thus the CO pathway is not fully suppressed and CO poisoning still occurs[11,14,15]. Therefore, HEA catalysts are limited by the trade-off between the needs for contiguous Pt atoms to enhance MOR activity and isolated Pt atoms to suppress CO poisoning. Developing catalysts with atomically dispersed Pt sites, high MOR activity, and strong resistance to CO poisoning remains highly desirable but challenging.

Here we report high-entropy alloyed single-atom Pt (denoted hereafter as HEASA-Pt), which behaves as an active MOR catalyst without suffering from CO poisoning. Our design combines the high activity of the HEA structure and anti-CO poisoning capability resulting from the single-atom Pt sites in the alloy lattice. The designed HEASA-Pt, Pt_1-NiCoMgBiSn, exhibits a notable mass activity of 35.3 A mg^{-1} (at 2.3 at% Pt), which is much higher than the activities of other MOR catalysts and commercial SA-Pt on carbon substrates (SA-Pt@C). Such high activity originates from the synergistic effect of multi-element coordination at each single-atom Pt site in Pt_1-NiCoMgBiSn. The HEASA-Pt catalyst maintains high mass activity even after operation for 180,000 s, demonstrating good durability. In-situ Fourier transform infrared (FT-IR) spectroscopy and CO stripping tests reveal the good anti-CO poisoning capability of HEASA-Pt. Density functional theory (DFT) calculations indicate that the high-entropy design modifies the coordination environment and electronic structure of HEASA-Pt, which weakens *CO adsorption and facilitates the HCOOH pathway simultaneously, thereby accelerating the MOR and suppressing CO poisoning.

Results

Design and synthesis of HEASA-Pt

Rapid cooling is essential to construct HEAs. In this work, HEASA-Pt was synthesized by an in-situ Joule-heating method using carbon nanotube (CNT) films, which reached a cooling rate of over 1000 °C/s[28]. The CNT films, which were used as both the heat source and substrate, were obtained through vacuum filtration of super-aligned CNTs[29,30]. Precursors including metal chlorides/chlorometal acids were dip coated on a CNT film. The CNT film coated with the metal precursors was rapidly Joule-heated to ~1100 °C by applying a certain voltage in a mixed atmosphere of 10% H_2/90% Ar. After several seconds, the heating voltage was removed, which caused the CNT film to naturally cool very rapidly (Supplementary Fig. 1), resulting in the growth of single-phase HEA nanoparticles on the CNT film. Refer to the Methods section for further details.

Theoretically, if the content of Pt is very low, most of the Pt atoms will exist in the form of isolating atomic sites in high entropy alloys rather than form Pt-Pt bonds with each other (Fig. 1a). It is worth noting that the HEASA-Pt can be synthesized only when the Pt content in precursor is very low (<4 at% relative to all metal elements). When the Pt content in precursor gets higher (>5 at%), the probability of forming contiguous Pt atoms increases and the product will be typical Pt-contained high-entropy alloy nanoparticles (hereafter denoted as HEA-Pt), in which Pt atoms may bond to each other. To obtain other coordination elements, DFT calculations were performed to establish a foundation for the design of HEASA-Pt with enhanced activity and durability, focusing on the adsorption energy of key intermediates in MOR. As the first order of approximation, we introduced a doping Co/Ni/Bi/Sn atom onto Pt(111) surface to evaluate the individual contribution from each kind of element in HEASA-Pt (Supplementary Fig. 2). Co and Bi have been reported to promote electron transfer in catalysts, lowering the oxidation energy barrier of *CO and facilitating the MOR[23,31]. Ni and Sn can act as oxyphilic elements to enhance the adsorption of OH^-, thereby accelerating the oxidation of *CO and improving the anti-CO poisoning ability of catalysts[24,32]. The effects of the alloying elements could be separated into two categories. On the one hand, modification of the coordination environment around Pt influences its reactivity. As shown in Fig. 1b, doping with a Bi or Sn atom weakened CO binding on adjacent Pt sites, suppressing CO poisoning, which is a well-known degradation mechanism of Pt-based MOR catalysts. On the other hand, coordination elements surrounding Pt may act as reactant donors or even new active sites, as well as dispersants and electronic-structure modulators. As demonstrated in Fig. 1c, OH adsorption on Co, Ni, or Sn is comparable to that on Pt, and thus these dopants can potentially serve as OH donors to supply sufficient OH species to MOR intermediates at active Pt sites, thereby facilitating oxidation processes. Additionally, the similar *CO adsorption on Co and Pt sites may assist in transferring CO from Pt to Co sites, where it can be oxidized by reaction with OH species on Co, thus promoting the reaction cycle at Pt sites. Moreover, we found that Mg doping would lead to a more negative valence state of Pt (Supplementary Fig. 3). Therefore, Mg was chosen as an electron-donor element to increase the electron density around Pt sites, thus weakening the adsorption of potentially poisoning carbonaceous species. Notably, Bi can have different effects on the catalyst[33,34]. When the Bi content is low, Bi can form $BiO_x(OH)_y$–Pt inverse interfaces to promote the MOR process. However, when the Bi content is too high, excess Bi species can aggregate and block Pt sites, degrading the MOR performance of catalysts[15,33]. As a result, the Bi content should be moderate. Consequently, HEASA-Pt was constructed from Co, Ni, Sn, Bi, Mg, and a small amount of Pt.

Characterization of HEASA-Pt

Aberration-corrected high-angle annular dark-field scanning transmission electron microscopy (HAADF-STEM) and corresponding energy-dispersive spectrometry (EDS) elemental mapping were first used to characterize the formation of single-atom Pt sites in HEASA-Pt (Fig. 2a, Supplementary Fig. 4 and 5). The EDS elemental mapping images show that all six elements are distributed homogeneously in large and small nanoparticles of HEASA-Pt. In particular, Pt is present at very sparse locations across an entire nanoparticle especially in the thinner edge regions, implying atomic-level distribution. There are some bright isolated spots in the HAADF-STEM images (Supplementary Fig. 6), suggesting that the elements with high atomic number, such as Pt or Bi (which are difficult to distinguish), likely to exist in the form of single atom sites. Inductively coupled plasma–optical emission spectroscopy (ICP-OES) was used to determine the elemental contents of HEASA-Pt and HEA-Pt. ICP-OES confirmed that the optimized HEASA-Pt catalyst contained all the six elements (Pt, Co, Ni, Sn, Bi, and Mg) with the Pt content of only 2.3 at% (Supplementary Tables 1 and 2).

We further conducted X-ray absorption fine structure (EXAFS) and X-ray absorption near-edge structure (XANES) measurements to investigate the coordination environment of Pt atoms in the HEASA-Pt. The intensity of the white line of Pt L_3-edge XANES of HEASA-Pt and HEA-Pt was slightly higher than that of Pt foil but much lower than that of PtO_2, indicating that Pt in the HEAs is mainly in a metallic state rather than an oxidized form (Fig. 2b). The EXAFS spectrum of HEASA-Pt shows a broad peak, which should be caused by the interaction of multiple elements around Pt. By contrast, the EXAFS spectrum of HEA-Pt appears more similar to that of Pt foil (Fig. 2c). To verify whether Pt atoms are isolated in HEASA-Pt, we fitted the magnitude of the Fourier transform of the k_3-weighted EXAFS data. The data used for the EXAFS

https://doi.org/10.1038/s41467-025-61376-y

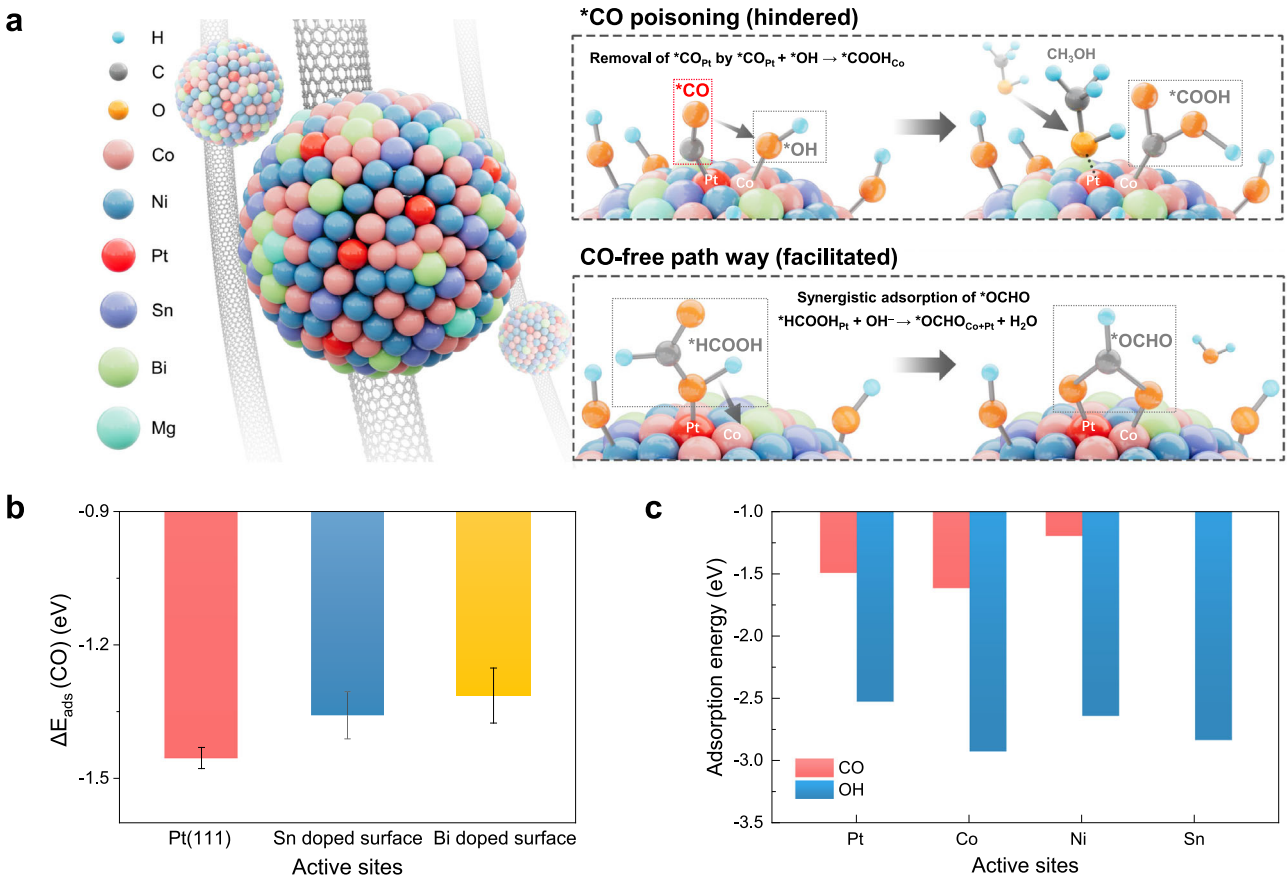

Fig. 1 | Design of HEASA-Pt as an MOR catalyst. a Schematic illustration of HEASA-Pt nanoparticles on CNTs and the corresponding MOR mechanism. Red dashed circles indicate the Pt atoms existing in single-atom state in the high-entropy lattice. The symbol * denotes adsorption and the subscript (Pt, Co, or Co + Pt) indicates adsorption sites. **b** Comparison of adsorption energies of CO intermediate on Pt(111) surface and doped Pt(111) surfaces with Sn and Bi. For the doped surfaces, only adsorption sites within the first coordination shell of doping atoms are considered. The error bars represent standard deviations. **c** Comparison of adsorption energies of CO and OH intermediates in MOR on Pt site and other doping Co/Ni/Sn atop sites. Source data for Fig. 1b–c are provided as a Source Data file.

fitting are provided in Supplementary Fig. 7 and Table 3. The coordination number of Pt-Pt in HEASA-Pt obtained from the fitting was 1.2 ± 0.3 (Fig. 2d and e and Supplementary Table 4), suggesting that there are few or no Pt-Pt bonds in HEASA-Pt. Wavelet transforms (WTs) of EXAFS spectra also revealed the absence of Pt as coordination atoms at Pt sites of HEASA-Pt. This is because neither strong Pt-Pt nor Pt-O coordination was observed in the WT contour plots of HEASA-Pt (Fig. 2g). By contrast, the EXAFS fitting results for HEA-Pt gave a high coordination number of Pt-Pt (4.4 ± 0.2) and decreased coordination numbers of other elements (Fig. 2d and f and Supplementary Table 4). Strong Pt-Pt coordination was also observed in the WT contour plots of HEA-Pt. Except for the strong Pt-Pt coordination, the WT contour plots of HEA-Pt were similar to those of HEASA-Pt because of their similar high-entropy lattice structures, but both of them differed greatly from those of Pt foil and PtO_2.

The morphology of HEASA-Pt was observed with transmission electron microscopy (TEM) and scanning electron microscopy (SEM). As shown in Supplementary Fig. 8–10, the as-synthesized catalyst particles were uniformly distributed on CNTs and exhibited nanoscale sizes. Most nanoparticles had diameters of less than 7 nm, averaging ~3 nm (Supplementary Fig. 9). At each magnification, no obvious core–shell structures were observed (Supplementary Fig. 6 and 8). An X-ray diffraction (XRD) pattern of HEASA-Pt showed two peaks at around 43.8° and 51.2°, which were assigned to the (111) and (200) facets, respectively, of a face-centered cubic phase (Supplementary Fig. 11). No other peaks were observed in the XRD pattern, meaning that HEASA-Pt consisted of a single phase. The lattice constant of HEASA-Pt was calculated to be ~3.6 Å, confirming the formation of an alloy phase. Spherical aberration-corrected transmission electron microscopy (AC-TEM) showed that the (111) interplanar distance of HEASA-Pt was about 2.1 Å and the {111} planes had an angle of 70.5° (Supplementary Fig. 12), consistent with the (111) interplanar distance calculated from XRD results. As the Pt content increased and the product changed from HEASA-Pt to HEA-Pt, the XRD peaks shifted to smaller angle because of the relatively large atomic radius of Pt, indicating a larger lattice constant (Supplementary Fig. 11). The HAADF-STEM and EDS elemental mapping images revealed the homogeneous distribution of Pt, Mg, Bi, Sn, Co, and Ni in both HEASA-Pt and HEA-Pt (Supplementary Fig. 13 and 14). X-ray photoelectron spectroscopy (XPS) also confirmed the presence of all six elements in both samples. As shown in Supplementary Fig. 15, Pt^0 $4f_{7/2}$ and Pt^0 $4f_{5/2}$ peaks appeared at 71.7 and 74.7 eV, respectively, indicating that Pt mainly exists in a metallic state, which is consistent with the XANES results.

MOR electrocatalytic performance and DMFC measurements

The electrochemical performance of the catalysts was measured using a three-electrode configuration with the as-synthesized HEASA-Pt/CNT and HEA-Pts/CNT films as working electrodes. Cyclic voltammetry (CV) curves of HEASA-Pt in 1 M KOH (Supplementary Fig. 16) showed obvious redox peaks of Bi at around −0.5 and −0.7 V[33]. As the number of CV cycles increased, the two redox peaks of Bi weakened, which should result from the surface reconstruction and stabilization of Bi on the catalyst surface during cycling. Figure 3a shows CV curves of samples with different Pt contents in a mixed solution of 1 M KOH and 1 M

https://doi.org/10.1038/s41467-025-61376-y

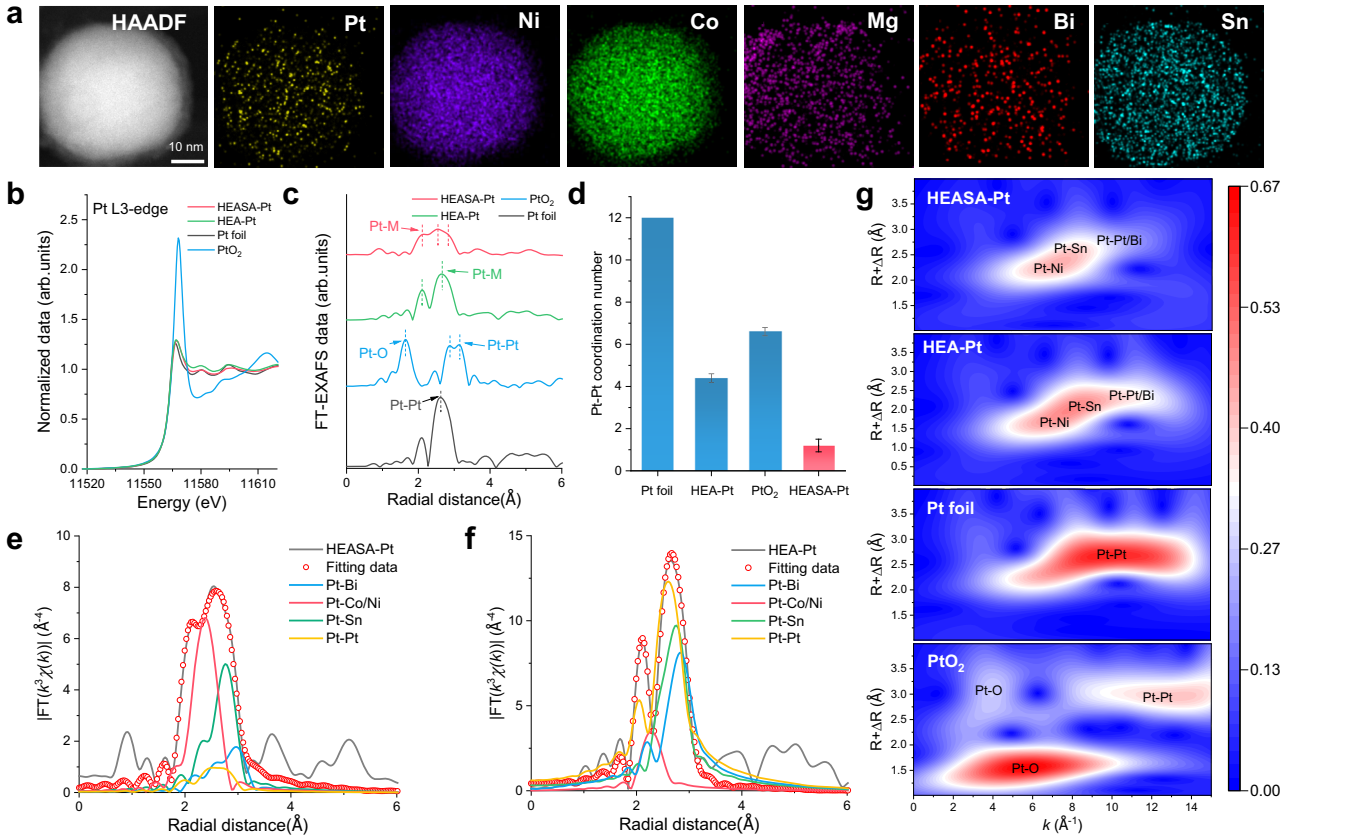

Fig. 2 | Structural characterization of HEASA-Pt$_{2.3\%}$, Pt$_1$-NiCoMgBiSn. **a** Aberration-corrected HAADF-STEM image of an HEASA-Pt nanoparticle and EDS mapping images of each element in HEASA-Pt. **b** XANES of HEASA-Pt$_{2.3\%}$, HEA-Pt$_{17.6\%}$, Pt foil, and PtO_2 at the Pt L_3-edge. **c** FT-EXAFS of HEASA-Pt$_{2.3\%}$, HEA-Pt$_{17.6\%}$, Pt foil, and PtO_2 at the Pt L_3-edge. **d** Comparison of the Pt-Pt coordination number of Pt foil, HEA-Pt, PtO_2, and HEASA-Pt. The error bars represent standard deviations generated by the least-squares method. Fitting results of the magnitude of the Fourier transform of the k_3-weighted EXAFS spectra for **e** HEASA-Pt$_{2.3\%}$ and (**f**) HEA-Pt$_{17.6\%}$. **g** WTs of EXAFS spectra of HEASA-Pt$_{2.3\%}$, HEA-Pt$_{17.6\%}$, Pt foil, and PtO_2. Source data for Fig. 2b–g are provided as a Source Data file.

methanol. In the forward scan, HEASA-Pt had an onset potential around 0.5 V vs. RHE and the current rapidly increased to a peak value at about 0.8 V vs. RHE, which was lower than the peak potentials of Pt/C and HEA-Pt (around 0.85–0.9 V vs. RHE). The MOR mass activity of the catalysts increased as the Pt content decreased from 17.6 to 3.1 at% and remained almost unchanged when the Pt content was ≤3.1 at% (Fig. 3b), where HEASA-Pt is considered to have been constructed. The HEASA-Pt catalysts with Pt contents of 1.1–3.1 at% exhibited notable MOR mass activity exceeding 30 A mg^{-1}, and when the Pt content is 2.3 at%, the HEASA-Pt$_{2.3\%}$ has the highest mass activity, 35.3 A mg^{-1}, outperforming commercial Pt/C catalyst (1.56 A mg1), SA-Pt@C (almost no catalytic activity), and HEA-Pt with higher Pt contents (3.65–17.6 A mg^{-1}) (Fig. 3(a,b), Supplementary Figs. 17–19). These results suggest that the HEASA-Pt catalysts exhibit high mass activity at a low Pt content, which is comparable to other SA-Pt and state-of-the-art MOR catalysts (Supplementary Fig. 20, Supplementary Tables 5 and 6)[13,15,16,20,22–24,32,33,35–41]. Moreover, because some elements besides Pt, including Pd, Rh, and Co, are also expensive, and thus we considered the cost of all metal precursors when calculating the cost activity (A/$). As shown in Supplementary Fig. 21, our HEASA-Pt achieved a higher cost activity than other state-of-the-art Pt-containing catalysts. This result reveals that HEASA-Pt is cost-effective because of the single-atom distribution of Pt in the high-entropy lattice.

Long-term activity is desirable for MOR catalysts. In addition to CO poisoning and mass transfer problems, the inevitable precipitation of carbonate or bicarbonate on the catalyst surface and the induced pH changes can degrade the activity of MOR catalysts[5]. We measured the activity of HEASA-Pt$_{2.3\%}$ by conducting a long-term chronoamperometric (CA) test at 0.7 V vs. RHE. As shown in Supplementary Fig. 22, after testing for 20,000 s, HEASA-Pt$_{2.3\%}$ maintained a mass activity of 1.3 A mg^{-1}, which was much higher than that of commercial Pt/C. Catalyst stability was not improved by promoting mass transfer through stirring (Supplementary Fig. 23). Therefore, the decrease of current during CA testing did not result from mass transfer limitations but was caused by the precipitation of carbonate or bicarbonate on the catalyst surface or by pH changes.

To comprehensively evaluate catalyst activity, we calculated the integral activity, which represents the amount of methanol oxidized per unit mass of Pt, of HEASA-Pt$_{2.3\%}$ by integrating the Pt mass-normalized i-t curve over time, and obtained the values over periods of 5000, 10,000, and 20,000 s. HEASA-Pt$_{2.3\%}$ showed higher integral activities than other Pt-containing MOR catalysts for all three periods (Supplementary Fig. 24), suggesting that HEASA-Pt maintains relatively higher activity over a long duration. The loss of Pt from the sample during CA measurements was evaluated by comparing the ICP-OES results with/without the CA tests. The results in Supplementary Fig. 25 indicate that there was no apparent Pt loss during the CA tests, which authenticates the measured mass activities.

Activity restoration is essential for the long-term electrochemical durability of MOR catalysts. It was found that if a few CV cycles were applied or the electrolyte was replaced with fresh 1 M KOH and 1 M methanol, the activity of HEASA-Pt$_{2.3\%}$ was well restored (Supplementary Figs. 26 and 27). We then conducted nine cycles of continuous CA tests for 20,000 s each on the same sample. The electrolyte was refreshed after each test. As shown in Fig. 3c, the current density fully recovered to its initial value after each test, suggesting the complete restoration of activity. Even after nine cycles (180,000 s in total), the

https://doi.org/10.1038/s41467-025-61376-y

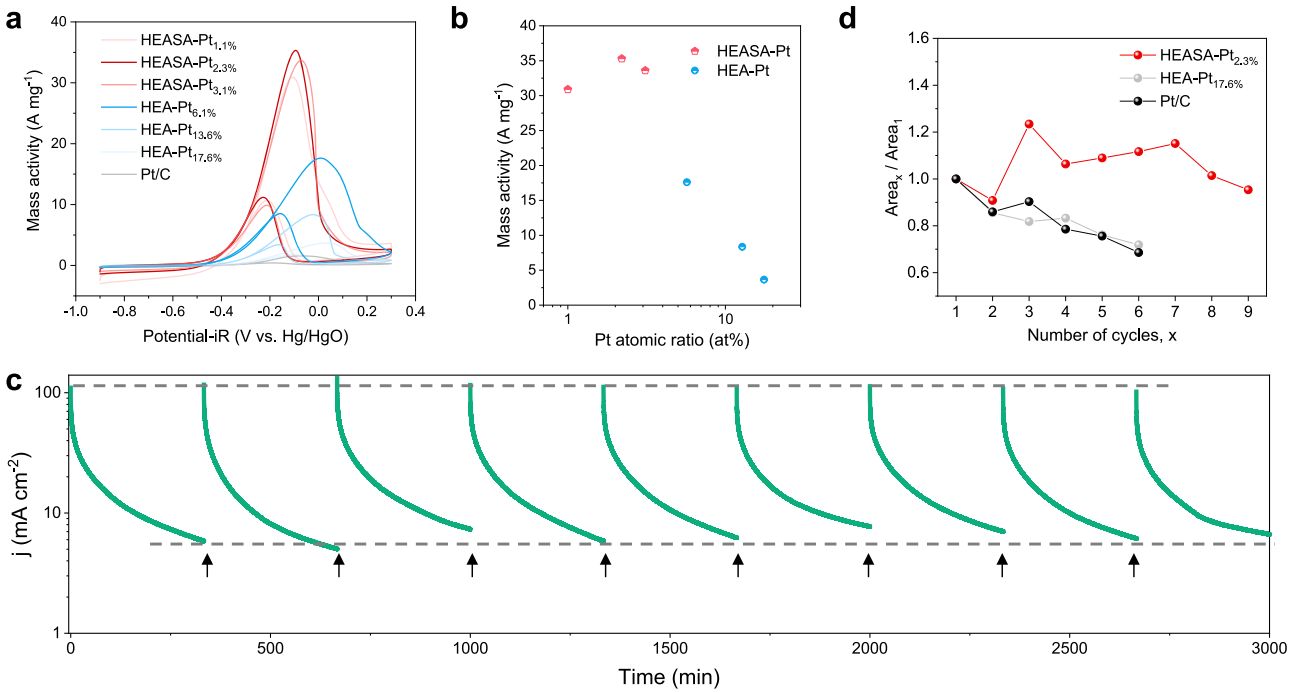

Fig. 3 | Electrocatalytic performance of HEASA-Pt for MOR. a CV curves of a series of HEASA-Pt and HEA-Pt catalysts with different Pt contents compared with those of commercial 20 wt% Pt/C. **b** Relationship between MOR mass activity and Pt contents of catalysts. **c** Long-term current density (*j*) measurements of HEASA-$Pt_{2.3\%}$. Arrows indicate when the electrolyte was refreshed. **d** $Area_{i\text{-}t}$ of HEASA-$Pt_{2.3\%}$, HEA-$Pt_{17.6\%}$, and Pt/C during the long-term durability test. Source data for Fig. 3a–d are provided as a Source Data file.

current at 0.7 V vs. RHE and CV peak current of the sample retained 94.7% and 83.4% of their initial values, respectively (Fig. 3d and Supplementary Fig. 28), demonstrating the good durability and renewability of HEASA-$Pt_{2.3\%}$. Notably, the phase structure and morphology of HEASA-$Pt_{2.3\%}$ remained almost unchanged after the long-term CA test, as revealed by the identical XRD patterns and SEM morphology before and after testing (Supplementary Figs. 29 and 30).

To better illustrate the durability of HEASA-$Pt_{2.3\%}$, we conducted the same series of CA tests on both Pt/C and HEA-$Pt_{17.6\%}$ (Supplementary Figs. 31 and 32). We calculated the starting current (I_{start}), ending current (I_{end}), and integrated area of the i-t curve ($S_{i\text{-}t}$, proportional to the total amount of methanol oxidized during the test) for each sample. As shown in Fig. 3d and Supplementary Fig. 33, all three parameters decreased considerably for Pt/C, possibly because of the severe poisoning of Pt in the long-term tests. For HEA-Pt, although I_{start} was recoverable, both I_{end} and $S_{i\text{-}t}$ decayed substantially, resulting in a decrease in the amount of methanol that can be oxidized during the test period, which means that HEA-Pt is also prone to poisoning. Conversely, these three parameters remained high for HEASA-$Pt_{2.3\%}$, indicating that it shows milder degradation of MOR performance over a long period than the other MOR catalysts (Fig. 3e and Supplementary Fig. 34). In addition, the performance of HEASA-$Pt_{2.3\%}$ did not degrade much until it was used for 200,000 s, which is considered the end-of-life of this catalyst (Supplementary Figs. 35). Compared with other MOR catalysts, HEASA-Pt showed the longest working time, further validating its good durability (Supplementary Fig. 36). Overall, HEASA-Pt is superior to other MOR catalysts in terms of lifespan, activity, cost, preparation efficiency, and environmental friendliness (Supplementary Fig. 37), which means that it demonstrates potential as a green and sustainable catalyst.

We conducted DMFC studies to further demonstrate the advantages of HEASA-Pt. Two types of alkaline DMFCs with a PBI membrane were tested. One was equipped with HEASA-Pt as the anode and commercial Pt/C as the cathode, and the other with Pt/C as both anode and cathode. Supplementary Fig. 38 shows the polarization and power density curves of the DMFCs obtained with O_2 as a cathodic gas feed and CH_3OH (1 M) as an anodic fuel feed in 6.0 M KOH electrolyte at 80 °C. The DMFC with the HEASA-Pt anode reached a peak power density of 22.8 mW cm^{-2}, which was higher than that reached by the DMFC with a commercial Pt/C anode (17.2 mW cm^{-2}). Notably, the former contained a low Pt content of 0.08 mg cm^{-2} whereas that of the latter was 0.4 mg cm^{-2}. When the Pt content of the HEASA-Pt anode was decreased to 0.04 mg cm^{-2}, the peak power density of the DMFC reached 13.0 mW cm^{-2} (Supplementary Fig. 39). By contrast, the DMFC with a Pt/C anode with a lower Pt content of 0.16 mg cm^{-2} hardly discharged. Regarding stability, the DMFC with an HEASA-Pt anode exhibited stable current density for 32,000 s under a cell voltage of 0.4 V (Supplementary Fig. 40). All of these results demonstrate that HEASA-Pt is superior to Pt/C in DMFCs because of its high power density, low Pt content, and good stability. Overall, HEASA-Pt shows potential for use as a low-cost, high-performance anode catalyst for DMFCs.

Reaction mechanism

To investigate the origin of the high MOR mass activity of HEASA-Pt, we performed in-situ Fourier transform infrared (FTIR) spectroscopic measurements to detect adsorbed intermediates at the molecular level during the MOR process. Figure 4a, b show the FTIR spectra of HEASA-$Pt_{2.3\%}$ and HEA-$Pt_{17.6\%}$, respectively, recorded from −0.7 to 0.5 V vs. Hg/HgO in 1 M KOH + 1 M methanol. The two catalysts showed different reaction pathways. For HEASA-$Pt_{2.3\%}$, the OCO antisymmetric stretching vibration band at around 1620 cm^{-1} appeared at −0.5 V vs. Hg/HgO and intensified with increasing potential. At higher potential, the C − OH and OCO symmetric stretching vibration bands between 1300 and 1400 cm^{-1} of *COOH emerged, suggesting that methanol was first oxidized to *COOH[13]. The bands at around 1540 cm^{-1} can be attributed to absorbed CO_3^{2-} [42,43], corresponding to the complete oxidation of methanol. It is worth noting that during the entire process, HEASA-$Pt_{2.3\%}$ did not display a CO adsorption peak, which is expected to lie between 1950 and 2100 cm^{-1} [12,44], during the entire process, indicating

https://doi.org/10.1038/s41467-025-61376-y

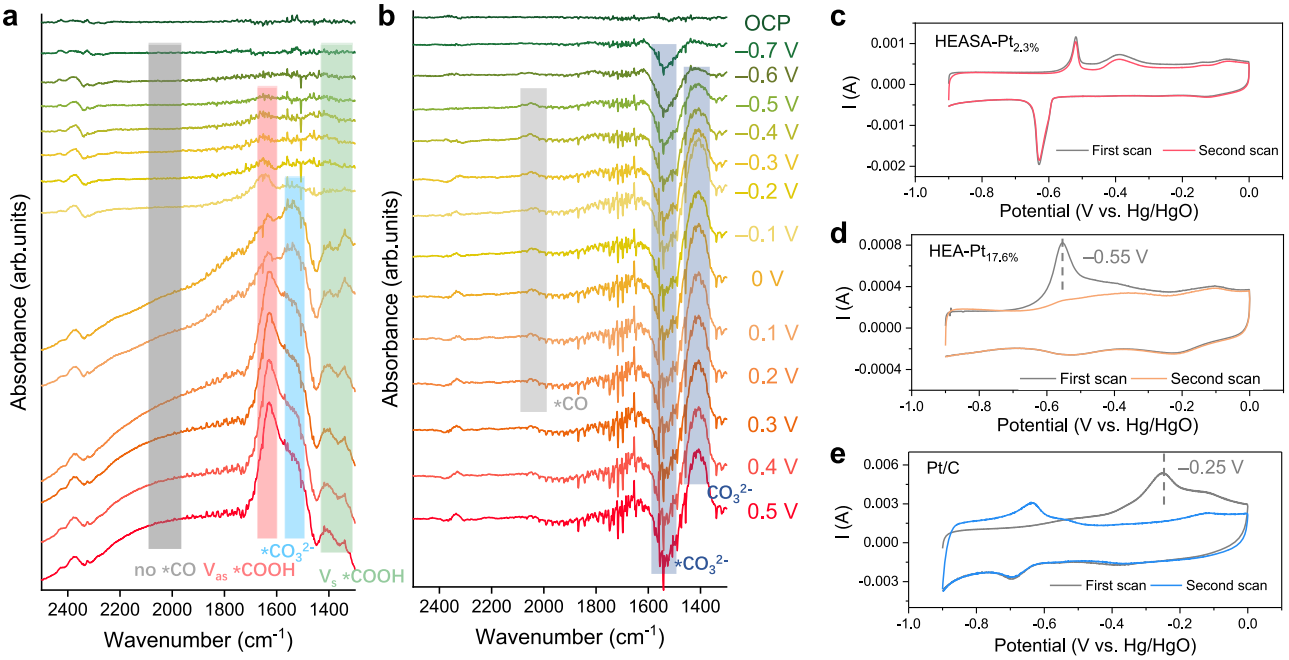

Fig. 4 | Experimental investigation of the MOR processes of different catalysts. In-situ FTIR spectra of (**a**) HEASA-$Pt_{2.3\%}$ and (**b**) HEA-$Pt_{17.6\%}$ at different potentials using a Hg/HgO as a reference electrode. CO stripping curves (no iR compensation) of (**c**) HEASA-$Pt_{2.3\%}$, (**d**) HEA-$Pt_{17.6\%}$, and (**e**) Pt/C catalysts for consecutive two scans (first scan and second scan). Source data for Fig. 4a–e are provided as a Source Data file.

that the reaction occurred through CO-free pathways[15,45]. As for the HEA-$Pt_{17.6\%}$, however, an obvious *CO signal is detected at 2049 cm^{-1} when the potential reached −0.5 V vs. Hg/HgO, which indicates that HEA-$Pt_{17.6\%}$ followed the CO pathway in a similar manner to Pt/C (Supplementary Fig. 41). A CO_2 vibration band at ~2335 cm^{-1} appeared at −0.3 V vs. Hg/HgO and intensified with increasing potential, corresponding to the further oxidation of *CO to CO_2, suggesting that HEA-$Pt_{17.6\%}$ catalyzes a different reaction pathway to that of HEASA-$Pt_{2.3\%}$. This comparison indicates that the atomically isolated Pt in HEASA-Pt prevents the catalyst from providing CO adsorption sites, which can thereby suppress CO poisoning and promote the MOR process. In addition, the valley in the FTIR spectrum of HEA-$Pt_{17.6\%}$ from 1400 to 1700 cm^{-1} (with a peak at around 1544 cm^{-1}) can be assigned to adsorbed carbonate anions with two oxygen atoms coordinated on the bridge site, and the band at ~1404 cm^{-1} can be assigned to carbonate anions in the solution[43]. The absence of a $*CO_3^{2-}$ adsorption band in the FTIR spectra of HEASA-$Pt_{2.3\%}$ may be caused by the lack of Pt-Pt bridge sites. Moreover, HEASA-Pt shows lower frequency O–H absorption peak at around 3236 cm^{-1} than that of Pt/C at around 3370 cm^{-1} (Supplementary Fig. 42). The low-frequency O–H absorption peak originates from the substantial adsorption of OH^- on HEASA-Pt and the formation of a large number of intermolecular hydrogen bonds between *OH[46], proving its good OH^- affinity. As for Pt/C, the number of *OH is not as many as that in HEASA-Pt and can only form fewer intermolecular hydrogen bonds, and as a result, the OH^- absorption peak of Pt/C appears at a higher frequency position.

We also conducted differential mass spectrometry (DEMS) measurements during methanol oxidation at 0.7 V vs. RHE in 1 M KOH + 1 M CH_3OH to identify intermediates based on the mass charge ratio (m/z). As shown in Supplementary Fig. 43, after applying a voltage, the signal intensity of methanol (m/z = 31) decreased considerably, indicating the consumption of methanol, whereas the signal intensity of formic acid and CO_2 (m/z = 46 and 44, respectively) increased. It is worth noting that the signal of CO_2 usually remarkably increases when it is abundantly produced at a high potential, e.g., after 0.9 V vs. RHE for commercial Pt/C, because the used KOH solution absorbs CO_2[47]. However, at 0.7 V vs. RHE, we observed a substantial increase of the CO_2 signal intensity, indicating that HEASA-Pt can effectively oxidize methanol to CO_2. We also collected signals of CO (m/z = 28). However, the signals at this mass charge ratio may also originate from fragments of methanol and CO_2[48]. During the testing process for 600 s, the signal of m/z = 28 does not accumulate and increase but significantly decreases due to the consumption of methanol, which also suggests that there was no CO generation. The above results indicate that at 0.7 V vs. RHE, the catalytic process of methanol on the HEASA-Pt surface is not affected by the CO poisoning, but is smoothly oxidized to formic acid and further oxidized to CO_2.

CO-stripping experiments were conducted to confirm this conclusion. As shown in Fig. 4c–e, oxidation peaks of absorbed CO were observed for HEA-$Pt_{17.6\%}$ and commercial Pt/C at about −0.55 and −0.25 V vs. Hg/HgO, respectively, but they are significantly suppressed on the HEASA-$Pt_{2.3\%}$. Moreover, HEASA-$Pt_{2.3\%}$ showed stable CV curves in CO-saturated 1 M KOH solution (Supplementary Fig. 44), further verifying its strong anti-CO poisoning capability. The CO oxidation peak potential of HEA-$Pt_{17.6\%}$ was lower than that of Pt/C because the alloying of multiple oxophilic elements promoted OH adsorption by HEA-Pt, which facilitated the removal of *CO via the L-H mechanism[5,7,49–51], thus enhancing the anti-CO poisoning ability of the high-entropy system. As the Pt content of HEA-Pt further decreases, Pt forms atomically isolated sites (less than three consecutive atoms) in high entropy alloys, i.e., HEASA-Pt, preventing CO from adsorbing on the catalyst surface and suppressing poisoning.

Furthermore, in order to elucidate the MOR reaction mechanism of HEASA-Pt, DFT calculations were performed using a representative HEASA-Pt model, as illustrated in Fig. 5a. Free-energy diagrams considering possible MOR pathways were calculated on the HEASA-Pt surface and compared with the results on a Pt(111) surface, as shown in Fig. 5b, c, respectively, with corresponding local structures provided in Supplementary Figs. 45 and 46. On the Pt(111) surface, oxidation of the CO intermediate was identified as the potential rate-determining step because of strong CO adsorption and poisoning, consistent with our expectation. By contrast, on the HEASA-Pt surface, CO adsorption weakened by more than 0.7 eV compared with that on Pt(111) (Fig. 5b, c), which is a larger decrease than that induced by the contribution of

https://doi.org/10.1038/s41467-025-61376-y

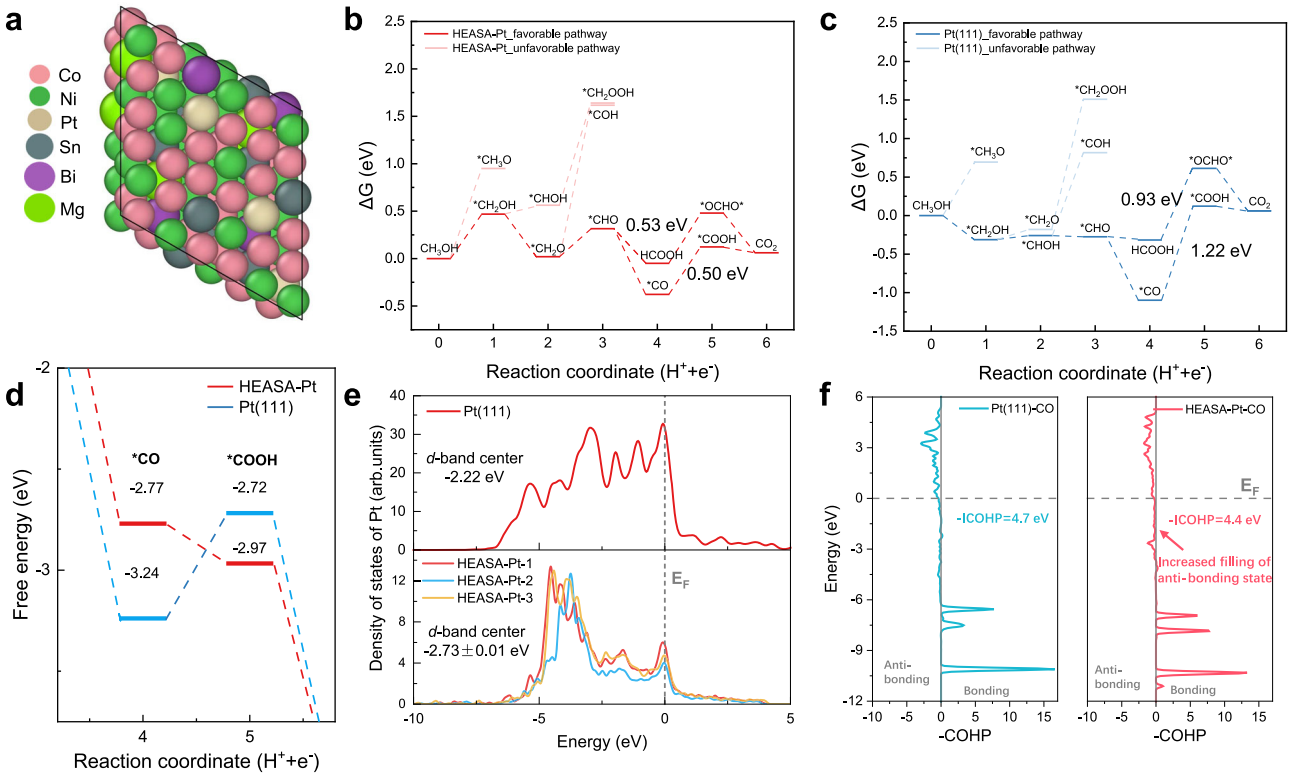

Fig. 5 | Theoretical analysis of the MOR processes on HEASA-Pt. a Exemplified HEASA-Pt surface slab model constructed for DFT calculations. Free-energy diagrams of possible pathways during the MOR on (**b**) HEASA-Pt and **c**, Pt(111) surfaces. **d** Comparison of the free-energy change of the CO oxidation step on HEASA-Pt and Pt(111) surfaces under an applied potential of 0.7 V vs. RHE. **e** Partial density of states of Pt in Pt(111) and HEASA-Pt. The dashed line represents the Fermi level, which is set as zero. **f** COHP results between Pt and C atoms (from CO) on Pt(111) and HEASA-Pt surfaces with the CO intermediate adsorbed on Pt sites. Source data for Fig. 5b–f are provided as a Source Data file.

any individual alloying element in Fig. 1c. In addition, CO adsorption on Co and Ni sites was mitigated by 0.66 and 0.67 eV, respectively, in HEASA-Pt compared with that in the binary systems (Supplementary Fig. 47). These results highlight the synergistic effect of the multiple elements in HEAs in suppressing CO adsorption. Moreover, CO adsorbed on isolated Pt sites of the HEASA-Pt surface can be effectively oxidized with the assistance of adjacent Co atoms, which facilitate the formation of *COOH intermediates, eventually leading to CO_2 formation. The thermodynamic energy difference of the oxidation step of *CO on the HEASA-Pt surface decreased to 0.50 eV, which can be easily overcome at the MOR working potential (higher than 0.6 V vs. RHE), thus avoiding CO poisoning (Fig. 5d and Supplementary Fig. 48).

In general, CO poisoning can be suppressed via two possible mechanisms: (1) enhancing CO oxidation reactivity to prevent CO accumulation on active sites, and/or (2) promoting an alternative reaction pathway that bypasses CO formation, such as the HCOOH pathway. Both mechanisms could be achieved simultaneously in our HEASA-Pt system. The high-entropy configuration not only weakens CO adsorption on Pt sites, but also stabilizes *COOH and *OCHO* intermediates with the help of adjacent oxophilic elements such as Co. The *OCHO intermediate is important in the HCOOH pathway. This alternative route could proceed with a low free-energy change of 0.52 eV on the HEASA-Pt surface, which is comparable to that of CO oxidation. By contrast, on a Pt(111) surface, that HCOOH pathway suffers from a higher energy difference of 0.93 eV. The occurrence of both MOR pathways on the HEASA-Pt surface explains why the CO intermediate was not detected on the HEASA-Pt surface as well as the high durability and MOR activity of HEASA-Pt.

We also explored the possibility of non-Pt sites (e.g., adjacent Co or Ni atoms) serving as active centers in the MOR. However, the results indicated that modified Pt remains the primary active site. Main-group elements such as Mg, Bi, and Sn exhibit negligible affinity for C-based intermediates such as *COOH and *CHO, and are thus catalytically inactive. Although Co and Ni can adsorb C-containing species, they suffer from strong CO binding and associated poisoning (Supplementary Fig. 49), similar to the case for Pt(111). As a result, the CO oxidation activity at Co and Ni sites is much lower than that at modified Pt sites. To further confirm the indispensable role of Pt in HEASA-Pt, we synthesized the Pt-free HEA BiMgSnCoNi. As shown in Supplementary Fig. 50, this alloy exhibited no MOR activity in 1 M KOH + 1 M CH_3OH, demonstrating that Pt is essential for catalytic function. Thus, the high performance of HEASA-Pt can be primarily attributed to the modified Pt sites embedded within the HEA matrix. This result also helps to explain the sustained supply of *OH species on the HEASA-Pt surface. Although neighboring atoms such as Co can act as synergistic reaction sites, potentially decreasing *OH availability, the overall favorable MOR energetics and compensatory contributions from other MOR-inactive alloying elements could help maintain a steady *OH supply.

From the electronic structure, we could further explain the origin of the changes in the reaction mechanisms. The *d*-band center of isolated Pt atoms on the HEASA-Pt surface was decreased compared with that on the Pt(111) surface (Fig. 5e and Supplementary Fig. 51), indicating a higher filling degree of *d*-orbitals of Pt after HEA formation, which is consistent with the crystal orbital Hamilton population (COHP) results shown in Fig. 5f. Analysis of the bonding characteristics between Pt and adsorbed CO showed that after alloying, more anti-bonding states are found between Pt and C, which weakens CO adsorption. Furthermore, the changes in electronic structure reflect the critical role of the HEA structure. On the one hand, the local stress around active sites could change the density of states, such as the compressive stress induced by Mg/Bi/Sn on nearby Pt compared to Pt(111), as shown in Fig. 5e. On the other hand, charge redistribution

between high-entropy elements changes the filling of new electronic structures, affecting adsorption of intermediates.

On the basis of their different roles in modifying electronic properties and catalytic reactivity, a qualitative distinction can be made between sub-group elements (Pt, Co, Ni) and main-group elements (Mg, Bi, Sn). As summarized in Supplementary Table 7, the charge redistribution across the HEASA-Pt systems reveals a consistent trend. Main-group elements (Mg, Bi, Sn) predominantly act as electron donors, transferring charge to the system, whereas sub-group elements, especially Pt, serve as electron acceptors and result in the increased occupancy of anti-bonding states in the Pt-CO interaction. Despite variations in local coordination environments, the *d*-band center of Pt remains relatively stable, underscoring the metallic nature and electronic resilience of the HEASA-Pt system.

To further validate these results, XPS analysis was conducted to investigate the redistribution of electron density around Pt sites in HEASA-Pt. As shown in Supplementary Fig. 52, Pt/C exhibits a higher Pt 4 f binding energy than that of HEASA-Pt, indicating that Pt has a more negative valence state in the latter than in the former. This result confirms that in HEASA-Pt, Pt serves as electron acceptor, consistent with theoretical findings. In addition, these trends remained for alternative high-entropy configurations in which individual alloying elements were selectively removed (Supplementary Fig. 53 and Supplementary Table 8). This further highlights the intrinsic robustness of the electron redistribution effect induced by the synergistic interactions of the elements in the HEA (detailed discussion is provided in the Supplementary Information).

Discussion

In summary, we design and synthesize a HEASA-Pt catalyst, Pt_1-NiCoMgBiSn, which introduces diverse alloy coordination elements while maintains the SA-Pt sites. The high-entropy structure of HEASA-Pt activated the intrinsically inactive SA-Pt sites, leading to high MOR catalytic activity. Moreover, the HEASA-Pt has a strong capability to resisted CO poisoning. It thereby combines the advantages of high activity originating from the high-entropy structure and anti-CO poisoning capability resulting from the SA-Pt sites in the alloy lattice. As a result, the HEASA-Pt exhibits notable MOR mass activity up to 35.3 A mg^{-1} at a Pt content of only 2.3 at%. After long-term durability tests, high electrochemical performance can be fully recovered through CV cycling or refreshing the electrolyte, which allowed the HEASA-Pt catalyst to maintain high mass activity even after operation for 180,000 s. In DMFC tests, HEASA-Pt output higher power density at lower Pt content than was the case for Pt/C and also exhibited good working stability, demonstrating its superiority to Pt/C as a DMFC anode catalyst. In-situ Fourier transform infrared (FTIR) spectra and DFT calculations revealed that the coordination of multiple alloying elements effectively weakened the binding between SA-Pt sites and CO in HEASA-Pt. Moreover, the synergistic effect between the SA-Pt sites and coordinating elements remarkably facilitates the oxidation of CO and thus avoids the CO-poisoning issue. Conversely, the HEA-Pt catalysts with high Pt content still suffered from CO poisoning, which led to relatively low activity and durability. Therefore, our HEASA-Pt exhibit notable activity and durability for MOR at a low Pt content. Our work demonstrates a universal high-entropy alloyed single-atom strategy to address CO poisoning of Pt-based MOR catalysts and will be beneficial for achieving high-efficiency DMFCs at low cost.

Methods

Syntheses of HEASA-Pt and HEA-Pt

The HEASA-Pt and HEA-Pt catalysts were synthesized by an ultrafast Joule-heating method with carbon nanotube (CNT) films as both the heating source and the supporting substrate[28]. The CNT films used for supporting and synthesizing HEASA-Pt and HEA-Pt were prepared by vacuum filtration of super aligned CNTs (SACNTs), which possess high purity, less defects, and very clean surfaces[29,30]. First, 20 mg SACNTs were dispersed in 200 mL ethanol by high-power probe ultrasonication (SCIENTZ-950E) at 600 W for 5 min. Afterwards, the suspension was vacuum filtrated using a suction filter, forming a CNT film. The CNT film was dried at 65 °C on a hot plate and then cut into rectangular-shape films using a laser (1064 nm in wavelength). Second, equal moles of $NiCl_2$ (Energy Chemical, 98%), $CoCl_2$ (Aladdin, 99.7%), $MgCl_2$ (3AChem, 99%), $BiCl_3$ (Meryer, AR), $SnCl_2$ (3AChem, 98%), and a certain amount of $H_2PtCl_6{\cdot}6H_2O$ (3AChem, Pt:37.5%) were dissolved in ethanol, and then dip-coated on the CNT films as precursors, followed by a drying process at 65 °C for 2 min. To prepare HEASA-Pt, the molar content of Pt in the precursor should be less than one fifth that of other elements (typically <4 at%). For HEA-Pt, the Pt content is greater than 5 at% (typically ranging from 6 to 18 at%) to meet the traditional definition of HEAs[52]. At last, the CNT film loaded with precursors was then clamped between two graphite electrodes, and a certain voltage was applied to the film to heat it up to about 1100 °C for 3 s in a mixed atmosphere of 10% H_2 and 90% Ar. The temperature of the CNT film during the growth was in situ measured by an infrared thermometer (Optrics, PI640). After that, the HEASA-Pt and HEA-Pt catalysts were synthesized on the CNT films and ready for characterizations and electrochemical measurements.

Characterization

Morphology of samples was observed by scanning electron microscopy (SEM; ZEISS, Merlin Compact), transmission electron microscopy (TEM; JEOL, JEM-2010F, 200 kV), and spherical aberration correction transmission electron microscopy (AC-TEM; JEOL, JEM ARM 200 F, 200 kV). TEM at different magnifications were also used for statistical analysis of particle sizes. Surface states of the samples were analysed by X-ray diffraction (XRD, D/max-2500/PC, Rigaku) with Cu Kα radiation ($\lambda = 0.15406$ nm) operated at 40 kV and 150 mA. X-ray photoelectron spectroscopy (XPS, Thermo Fisher, Escalab 250Xi, Al Kα) was carried out from 0 to 1350 eV at a step of 1 eV.

Electrochemical measurements

All electrochemical measurements were performed following a standard three-electrode test under CHI 660e and CHI 760e electrochemical workstations. The CNT films with HEASA-Pt or HEA-Pt nanoparticles directly served as the working electrodes (0.24 cm2), Hg/HgO as a reference electrode, and Pt as a counter electrode. Cyclic voltammograms (CVs) were performed in N_2-saturated 1 M KOH solution (pH = 14 ± 0.1) from −0.9 to 0.3 V vs. Hg/HgO ($E_{(RHE)} = E_{(Hg/HgO)} + 0.0591 \times pH + 0.098$) at a scan rate of 100 mV s^{-1} to activate the catalyst. For the MOR activity, the CVs were conducted in N_2-saturated 1 M KOH and 1 M methanol solution between −0.9 to 0.3 V vs. Hg/HgO at a scan rate of 50 mV s^{-1} with 85% iR compensation. All solutions were prepared using deionized water, KOH (Aladdin, GR), and methanol (Macklin, 99.9%) within 30 min of testing. After the CV cycle had stabilized, ICP-OES measurements were performed to precisely measure the Pt content of the catalyst. The mass activity was derived by dividing the current obtained from the final CV cycle by the mass of Pt. To assess long-term stability, CA tests were performed at a fixed potential of 0.7 V vs. RHE. After completing each test for 20,000 s, the electrolyte was refreshed. The Pt/C catalyst was prepared by dip coating CNT films in a solution of commercial 20 wt% Pt/C powder, Nafion (50 µL), ethanol (500 µL), and distilled water (450 µL). The loading content of Pt/C was ~0.75 mg cm^{-2}. In DMFC tests, a 2 cm × 2 cm HEASA-Pt/CNT film was prepared and directly used as the catalyst layer. The PBI membrane (35 µm) was treated sequentially at 60 °C in 6 M KOH solution for 3 h, 40 °C for 6 h, and finally left overnight in 6 M KOH solution before use.

CO stripping test

CO stripping tests were conducted in 1 M KOH solution. First, the potential of the working electrode was maintained at −0.9 V vs. Hg/

HgO while CO was bubbled into the solution for 30 min to form a CO monolayer on the catalysts. Then, N_2 was bubbled into the solution for 15 min to remove the dissolved CO. CV was conducted from −0.9 to 0 V vs. Hg/HgO at a scan rate of 10 mV s^{-1} for at least two cycles.

In situ FTIR measurements

In situ attenuated total reflection (ATR) FTIR electrochemical measurements were performed on a Linglu Instruments ECIR-II cell mounted on a Pike Veemax III ATR accessory with a single-bounce silicon crystal covered with a gold membrane in internal reflection mode. Spectra were recorded on a Thermo Nicolet Nexus 670 spectrometer. The in situ FT-IR spectra were collected from −0.7 to 0.5 V (vs. Hg/HgO) every 100 mV in N_2-saturated 1.0 M KOH + 1.0 M methanol.

XAFS measurements and data processing

XAFS spectra (Pt L_3-edge) were collected at the BL14W1 beamline of the Shanghai Synchrotron Radiation Facility (Shanghai, China). Data were collected in transmission mode using an ionization chamber for Pt foil and PtO_2 and in fluorescence excitation mode using a Lytle detector for HEASA-Pt. All spectra were collected under ambient conditions. The XAFS spectra were processed following standard protocols with IFEFFIT's Athena module. The EXAFS spectra were generated through post-edge background subtraction from the overall absorption, followed by normalization to the edge-jump step. The resulting χ(k) signals underwent Fourier transformation to real (R) space with a Hanning window (dk = 1.0 $Å^{-1}$), enabling separation of EXAFS contributions from different coordination shells. Quantitative structural parameters for the central atoms were then extracted through least-squares curve fitting implemented in the ARTEMIS module of IFEFFIT[53,54].

DFT calculations

DFT calculations were performed with the Vienna ab initio simulation package (VASP)[55]. Electron–ion interactions were described by the projector augmented wave method[56]. The revised Perdew–Burke–Ernzerhof functional within the generalized gradient approximation was used to describe exchange and correlation interactions[57]. The DFT-D3 method with zero damping was used to account for Van der Waals interactions[58]. All structures were optimized until the force on each atom was less than 0.03 eV $Å^{-1}$ and the self-consistent energy criterion was set to 10^{-5} eV. The supercell random approximates method, combined with Cuckoo search and Monte-Carlo simulation, was used to search for high-entropy structures with dispersed element distributions[59]. Three replicates were performed to avoid the results being a special case. The similarity of lattice constants and electronic structures demonstrates the generality of the constructed high-entropy models (Supplementary Fig. 54 and 55). Free-energy diagram calculations were conducted using p(3 × 3) (111) surfaces with three-layer slab models. An additional vacuum layer of 15 Å was added to each slab along the *z*-direction to avoid spurious interactions between images caused by the periodic boundary conditions. The energy cutoff for the plane wave basis expansion was set to 500 eV, and a 3 × 3 × 1 Monkhorst-Pack *k*-point grid was used to sample the Brillouin zone[60]. The VASPsol package was used to simulate the solvation environment[61,62]. COHP calculations were performed using the LOBSTER package[63].

A computational hydrogen electrode model was used to calculate the reaction free-energy change of each step of the MOR. The free-energy changes were calculated using Eq. (1):

$$\Delta G = \Delta E_{DFT} + \Delta ZPE - \Delta TS, \tag{1}$$

where G, E_{DFT}, ZPE, T, and S represent the Gibbs free energy, total energy from the DFT calculations, zero point energy, temperature (300 K), and entropy, respectively. The energy of $H^+ + e^-$ was related to H_2 according to the equilibrium at $U = 0$ V_{RHE}:

$$H^+ + e^- \leftrightarrow \frac{1}{2}H_2. \tag{2}$$

Data availability

The data supporting this study are available within the paper and the Supplementary Information. All other relevant source data are available from the corresponding authors upon reasonable request. The source data for Figs. 1–5 and Supplementary Figures are provided as a Source Data file. The DFT optimized structures used for electronic structure calculations are provided in the Supplementary Data 1. Source data are provided with this paper.

References

1. Nguyen, A. Q. K., Pham, H. Q., Huynh, S. T. M. & Huynh, T. T. Milestones of electrocatalyst development for direct alcohol fuel cells. *Adv. Sustain. Syst.* **7**, 2300205 (2023).
2. Seh, Z. W. et al. Combining theory and experiment in electrocatalysis: insights into materials design. *Science* **355**, eaad4998 (2017).
3. Chu, S. & Majumdar, A. Opportunities and challenges for a sustainable energy future. *Nature* **488**, 294–303 (2012).
4. Yuda, A., Ashok, A. & Kumar, A. A comprehensive and critical review on recent progress in anode catalyst for methanol oxidation reaction. *Catal. Rev.* **64**, 126–228 (2020).
5. Wang, J. et al. Toward electrocatalytic methanol oxidation reaction: longstanding debates and emerging catalysts. *Adv. Mater.* **35**, 2211099 (2023).
6. Anson, C. W. & Stahl, S. S. Mediated fuel cells: soluble redox mediators and their applications to electrochemical reduction of O_2 and oxidation of H_2, alcohols, biomass, and complex fuels. *Chem. Rev.* **120**, 3749–3786 (2020).
7. Fu, X., Wan, C., Huang, Y. & Duan, X. Noble metal based electrocatalysts for alcohol oxidation reactions in alkaline media. *Adv. Funct. Mater.* **32**, 2106401 (2022).
8. Tripkovíc, A. V. et al. Methanol electrooxidation on supported Pt and PtRu catalysts in acid and alkaline solutions. *Electrochim. Acta* **47**, 3707–3714 (2002).
9. Kabbabi, A. et al. In situ FTIRS study of the electrocatalytic oxidation of carbon monoxide and methanol at platinum-ruthenium bulk alloy electrodes. *J. Electroanal. Chem.* **444**, 41–53 (1998).
10. Alayoglu, S., Nilekar, A. U., Mavrikakis, M. & Eichhorn, B. Ru–Pt core–shell nanoparticles for preferential oxidation of carbon monoxide in hydrogen. *Nat. Mater.* **7**, 333–338 (2008).
11. Cuesta, A. At least three contiguous atoms are necessary for CO formation during methanol electrooxidation on platinum. *J. Am. Chem. Soc.* **128**, 13332–13333 (2006).
12. Li, M. et al. Sub-monolayer YO_x/MoO_x on Ultrathin pt nanowires boosts alcohol oxidation electrocatalysis. *Adv. Mater.* **33**, 2103762 (2021).
13. Zhu, J. et al. Ultrahigh stable methanol oxidation enabled by a high hydroxyl concentration on pt clusters/MXene interfaces. *J. Am. Chem. Soc.* **144**, 15529–15538 (2022).
14. Neurock, M., Janik, M. & Wieckowski, A. A first principles comparison of the mechanism and site requirements for the electrocatalytic oxidation of methanol and formic acid over Pt. *Faraday Discuss* **140**, 363–378 (2008).
15. Chen, W. et al. High-entropy intermetallic PtRhBiSnSb nanoplates for highly efficient alcohol oxidation electrocatalysis. *Adv. Mater.* **34**, 2206276 (2022).
16. Awoke, Y. A. et al. The synergistic effect Pt_1-W dual sites as a highly active and durable catalyst for electrochemical methanol oxidation. *Electrochim. Acta* **432**, 141161 (2022).

17. Kim, J., Kim, H. E. & Lee, H. Single-atom catalysts of precious metals for electrochemical reactions. *ChemSusChem* **11**, 104–113 (2017).
18. Shen, T., Wang, S., Zhao, T., Hu, Y. & Wang, D. Recent advances of single-atom-alloy for energy electrocatalysis. *Adv. Energy Mater.* **12**, 2201823 (2022).
19. Kim, Y. T. et al. Fine size control of platinum on carbon nanotubes: from single atoms to clusters. *Angew. Chem. Int. Ed.* **45**, 407–411 (2006).
20. Zhang, Z. et al. Single-atom catalyst for high-performance methanol oxidation. *Nat. Commun.* **12**, 5235 (2021).
21. Poerwoprajitno, A. R. et al. A single-Pt-atom-on-Ru-nanoparticle electrocatalyst for CO-resilient methanol oxidation. *Nat. Catal.* **5**, 231–237 (2022).
22. Wang, Y. et al. Synthesis of high-entropy-alloy nanoparticles by a step-alloying strategy as a superior multifunctional electrocatalyst. *Adv. Mater.* **35**, 202302499 (2023).
23. Li, H. et al. Fast site-to-site electron transfer of high-entropy alloy nanocatalyst driving redox electrocatalysis. *Nat. Commun.* **11**, 5437 (2020).
24. Yang, F. et al. Ultrathin PtNiGaSnMoRe Senary nanowires with partial amorphous structure enable remarkable methanol oxidation electrocatalysis. *Adv. Energy Mater.* **13**, 202301408 (2023).
25. Yao, Y. G. et al. Carbothermal shock synthesis of high-entropy-alloy nanoparticles. *Science* **359**, 1489–1494 (2018).
26. Yao, Y. et al. High-entropy nanoparticles: Synthesis-structure-property relationships and data-driven discovery. *Science* **376**, eabn3103 (2022).
27. Wang, B. et al. General synthesis of high-entropy alloy and ceramic nanoparticles in nanoseconds. *Nat. Synth.* **1**, 138–146 (2022).
28. Li, C. et al. Ultrafast self-heating synthesis of robust heterogeneous nanocarbides for high current density hydrogen evolution reaction. *Nat. Commun.* **13**, 3338 (2022).
29. Jiang, K., Li, Q. & Fan, S. Spinning continuous carbon nanotube yarns. *Nature* **419**, 801–801 (2002).
30. Zhang, X. et al. Spinning and processing continuous yarns from 4-inch wafer scale super-aligned carbon nanotube arrays. *Adv. Mater.* **18**, 1505–1510 (2006).
31. Chen, W. et al. Hexagonal PtBi Intermetallic inlaid with submonolayer pb oxyhydroxide boosts methanol oxidation. *Small* **18**, 2107803 (2022).
32. Li, M. et al. Single-atom tailoring of platinum nanocatalysts for high-performance multifunctional electrocatalysis. *Nat. Catal.* **2**, 495–503 (2019).
33. Fan, X. et al. Surface-enriched single-Bi-atoms tailoring of pt nanorings for direct methanol fuel cells with ultralow-Pt-loading. *Adv. Mater.* **36**, 2313179 (2024).
34. Li, X. et al. Interface-rich Au-doped PdBi alloy nanochains as multifunctional oxygen reduction catalysts boost the power density and durability of a direct methanol fuel cell device. *Nano Res* **15**, 6036–6044 (2022).
35. He, L. et al. Single-atom Mo-tailored high-entropy-alloy ultrathin nanosheets with intrinsic tensile strain enhance electrocatalysis. *Nat. Commun.* **15**, 2290 (2024).
36. Zhang, S. et al. Lanthanide electronic perturbation in Pt–Ln (La, Ce, Pr and Nd) alloys for enhanced methanol oxidation reaction activity. *Energy Environ. Sci.* **14**, 5911–5918 (2021).
37. Han, S. et al. The synergy of tensile strain and ligand effect in PtBi nanorings for boosting electrocatalytic alcohol oxidation. *Adv. Funct. Mater.* **32**, 202208760 (2022).
38. Liang, W. et al. 3D anisotropic Au@Pt–Pd hemispherical nanostructures as efficient electrocatalysts for methanol, ethanol, and formic acid oxidation reaction. *Adv. Mater.* **33**, 202100713 (2021).
39. Wang, X. et al. Bismuth oxyhydroxide-Pt inverse interface for enhanced methanol electrooxidation performance. *Nano Lett.* **20**, 7751–7759 (2020).
40. Shang, C., Guo, Y. & Wang, E. Integration of two-dimensional morphology and porous surfaces to boost methanol electrooxidation performances of PtAg alloy nanomaterials. *Nano Res.* **11**, 6375–6383 (2018).
41. Hui, L. et al. Highly loaded independent Pt^0 atoms on graphdiyne for pH-general methanol oxidation reaction. *Adv. Sci.* **9**, 2104991 (2022).
42. Heyes, J., Dunwell, M. & Xu, B. CO_2 reduction on Cu at low overpotentials with surface-enhanced in situ spectroscopy. *J. Phys. Chem. C.* **120**, 17334–17341 (2016).
43. Zhu, S., Jiang, B., Cai, W.-B. & Shao, M. Direct observation on reaction intermediates and the role of bicarbonate anions in CO_2 electrochemical reduction reaction on Cu surfaces. *J. Am. Chem. Soc.* **139**, 15664–15667 (2017).
44. Wang, W. et al. Quatermetallic Pt-based ultrathin nanowires intensified by Rh enable highly active and robust electrocatalysts for methanol oxidation. *Nano Energy* **71**, 104623 (2020).
45. Zhao, F., Ye, J., Yuan, Q., Yang, X. & Zhou, Z. Realizing a CO-free pathway and enhanced durability in highly dispersed Cu-doped PtBi nanoalloys towards methanol full electrooxidation. *J. Mater. Chem. A* **8**, 11564–11572 (2020).
46. Zhu, J. et al. Surface passivation for highly active, selective, stable, and scalable CO_2 electroreduction. *Nat. Commun.* **14**, 4670 (2023).
47. Xu, K. et al. $Pt_{1.8}Pd_{0.2}CuGa$ intermetallic nanocatalysts with enhanced methanol oxidation performance for efficient hybrid seawater electrolysis. *Adv. Mater.* **36**, 2403792 (2024).
48. Kim, C., Weng, L. C. & Bell, A. T. Impact of pulsed electrochemical reduction of CO_2 on the formation of C2+ products over Cu. *ACS Catal.* **10**, 12403–12413 (2020).
49. Spendelow, J. S., Goodpaster, J. D., Kenis, P. J. A. & Wieckowski, A. Mechanism of CO oxidation on Pt(111) in alkaline media. *J. Phys. Chem. B* **110**, 9545–9555 (2006).
50. Lee, M. J. et al. Understanding the bifunctional effect for removal of co poisoning: blend of a platinum nanocatalyst and hydrous ruthenium oxide as a model system. *ACS Catal.* **6**, 2398–2407 (2016).
51. Wu, X. et al. Tuning surface structure of Pd_3Pb/Pt_nPb nanocrystals for boosting the methanol oxidation reaction. *Adv. Sci.* **6**, 1902249 (2019).
52. Hsu, W. L., Tsai, C. W., Yeh, A. C. & Yeh, J. W. Clarifying the four core effects of high-entropy materials. *Nat. Rev. Chem.* **8**, 471–485 (2024).
53. Ravel, B. & Newville, M. ATHENA, ARTEMIS, HEPHAESTUS: data analysis for X-ray absorption spectroscopy using IFEFFIT. *J. Synchrotron Radiat.* **12**, 537–541 (2005).
54. Yao, Y. et al. Engineering the electronic structure of single atom Ru sites via compressive strain boosts acidic water oxidation electrocatalysis. *Nat. Catal.* **2**, 304–313 (2019).
55. Kresse, G. & Furthmüller, J. Efficient iterative schemes for ab initio total-energy calculations using a plane-wave basis set. *Phys. Rev. B* **54**, 11169–11186 (1996).
56. Kresse, G. & Joubert, D. From ultrasoft pseudopotentials to the projector augmented-wave method. *Phys. Rev. B* **59**, 1758–1775 (1999).
57. Hammer, B., Hansen, L. B. & Nørskov, J. K. Improved adsorption energetics within density-functional theory using revised Perdew-Burke-Ernzerhof functionals. *Phys. Rev. B* **59**, 7413–7421 (1999).
58. Grimme, S., Antony, J., Ehrlich, S. & Krieg, H. A consistent and accurate ab initio parametrization of density functional dispersion correction (DFT-D) for the 94 elements H-Pu. *J. Chem. Phys.* **132**, 154104 (2010).
59. Singh, R., Sharma, A., Singh, P., Balasubramanian, G. & Johnson, D. D. Accelerating computational modeling and design of high-entropy alloys. *Nat. Comput. Sci.* **1**, 54–61 (2021).
60. Monkhorst, H. J. & Pack, J. D. Special points for Brillouin-zone integrations. *Phys. Rev. B* **13**, 5188–5192 (1976).

61. Mathew, K., Sundararaman, R., Letchworth-Weaver, K., Arias, T. A. & Hennig, R. G. Implicit solvation model for density-functional study of nanocrystal surfaces and reaction pathways. *J. Chem. Phys.* **140**, 084106 (2014).
62. Mathew, K., Kolluru, V. S. C., Mula, S., Steinmann, S. N. & Hennig, R. G. Implicit self-consistent electrolyte model in plane-wave density-functional theory. *J. Chem. Phys.* **151**, 234101 (2019).
63. Maintz, S., Deringer, V. L., Tchougréeff, A. L. & Dronskowski, R. LOBSTER: A tool to extract chemical bonding from plane-wave based DFT. *J. Comput. Chem.* **37**, 1030–1035 (2016).

Acknowledgements

K.L. acknowledges the financial support from the National Key R&D Program of China (2022YFA1203400), National Natural Science Foundation of China (52272041), and Basic Science Center Project of NSFC (52388201). J.L. acknowledges the support from the National Key R&D Program of China (2022YFA1203400, 2021YFA1400100), National Natural Science Foundation of China (12274254), Local Innovative and Research Teams Project of Guangdong Pearl River Talents Program (2017BT01N111), Basic Research Project of Shenzhen, China (JCYJ20200109142816479, WDZC20200819115243002), and Shenzhen Outstanding Talents Training Fund. Computational calculations were supported by the High Performance Computing Platform of Nanjing University of Aeronautics and Astronautics.

Author contributions

K.L. and M.L. conceived the project and designed experiments. M.L. and C.L. synthesized samples. M.L., S.J. and K.Z. characterized samples. M.L. performed electrochemical measurements. J.L. and Z.Z. performed DFT calculations. M.L., K.L., J.L., Z.Z. and K.Z. analyzed the data. K.L., J.L., M.L., Z.Z. and S.F. discussed the working mechanism. M.L., K.L., Z.Z. and J.L. wrote and revised the manuscript. All authors discussed the results and contributed to the final version of the manuscript.

Competing interests

The authors declare no competing interests.

Additional information

Supplementary information The online version contains supplementary material available at https://doi.org/10.1038/s41467-025-61376-y.

Correspondence and requests for materials should be addressed to Jia Li or Kai Liu.

Peer review information *Nature Communications* thanks Sang-Jae Kim, Jamal Abdul Nasir, Deli Wang and the other anonymous reviewer(s) for their contribution to the peer review of this work. A peer review file is available.